

# Propagation of Cracks in Selected Specimens Subject to Mixed-Mode

G. Dhondt<sup>1</sup>, and D. Bremberg<sup>2</sup>

**Abstract:** In a previous article the K-distribution along the crack front of several mixed-mode specimens was investigated [Dhondt, Chergui, and Buchholz (2001)]. Both the modified virtual crack closure integral method and the quarter point element stress field method yielded results close to the available reference solutions in the literature [Murakami (1987)]. The present paper extends these results in two aspects. First, the meshing procedure used to obtain a focused mesh at the crack front is modified in order to deal with highly curved cracks. Secondly, the K-distribution along the initial crack is used to perform a crack propagation calculation. The form of the propagated cracks agrees well with what one expects and with experimental evidence.

**keyword:** Crack propagation, mixed-mode, curved cracks.

## 1 Introduction

Due to weight reduction and high temperatures crack initiation life is often not sufficient to meet lifing requirements. Therefore, crack propagation calculations are becoming more and more standard in the development phase of an aircraft engine component. Furthermore, crack propagation predictions can contribute significantly to the life extension of damaged parts. The complex loading usually leads to a mixed-mode state at the crack front, i.e. the crack is loaded both in tension and shear. This leads to complex crack propagation patterns, which have to be predicted. In the past, a lot of new software developments were applied to solve complex crack propagation shapes such as the boundary element method [Helldörfer (2009)], the partition of unity finite element method (PUFEM) [Melenk and Babuska (1996)] and meshless methods [Wen and Aliabadi (2010)][Belytschko, Lu, and Gu (1994)]. Although each of these methods has its merits, including more advanced phe-

nomena such as large deformations, nonlinear material behavior and 3-D temperature and residual stress fields usually proves quite difficult. In this paper, the classical finite element is taken. It is widely used and nearly every nonlinear phenomenon one can think of has been covered. The major drawback is that the complete volume of the cracked structure has to be meshed. Especially the introduction of the complex crack geometry represents a real challenge. In the past, a program with the name CRACKTRACER has been developed at MTU to cope with mode-I cracks. To this end, the uncracked structure was meshed with hexahedrons and a local remeshing near the crack generated a suitable focussed mesh at the front. In later years applications have shown that, although the method performed very well for mode-I cracks, the extension to mixed-mode cracks was not realistic. Therefore, an alternative approach was started four years ago, leading to the new software CRACKTRACER 3-D [Bremberg and Dhondt (2008)][Bremberg and Dhondt (2009)]. It generates a hexahedral tube along the crack front, while the remaining parts of the domain of interest are automatically filled with tetrahedrons. The radius of the tube is a monotonically decreasing function of the local curvature of the crack front. This more flexible approach was tested on specimens and real engine structures and proved to be very stable and reliable. In the present context, it is applied to the specimens which were analyzed in [Dhondt, Chergui, and Buchholz (2001)].

## 2 Outline of the method

The procedure used in CRACKTRACER 3-D has been described extensively in other publications [Bremberg and Dhondt (2008)]. Therefore, a short outline should suffice. The input to CRACKTRACER 3-D consists of a CalculiX [Dhondt and Wittig (1998–2010)] input deck of the uncracked structure, a file describing the initial crack geometry, a crack propagation data file and a file defining a limited volume of elements large enough to contain the crack. The requirements on the input deck of the un-

<sup>1</sup> MTU Aero Engines, Munich, Germany

<sup>2</sup> MTU Aero Engines, Munich, Germany and KTH Stockholm, Sweden

cracked structure are:

- the mesh must be three-dimensional
- the calculation must be linear
- only options available in CalculiX are allowed.

In particular, the mesh of the uncracked structure is only relevant to the extent that it should describe the geometry of the part in sufficient detail. At first, a flexible tube is generated with the crack front as trajectory line. The tube is filled with a structured and focussed 20-node hexahedral mesh. Intersection operations including the free boundary of the domain, the duplicated crack face and the flexible tube result in a geometric description of a transition region connecting the tubular mesh and the remaining input mesh that is not part of the defined domain. This transition region is automatically filled with an unstructured 10-node tetrahedral mesh by use of NETGEN [Schöberl (1997)]. The separate and dissimilar meshes are finally connected by multiple point constraints. This is clearly visible in Fig. 1. At the crack front the 20-node hexahedra are collapsed into quarter point elements. These exhibit the characteristic  $1/\sqrt{r}$  stress and strain singularity typical for linear elastic crack calculations [Barsoum (1976)].

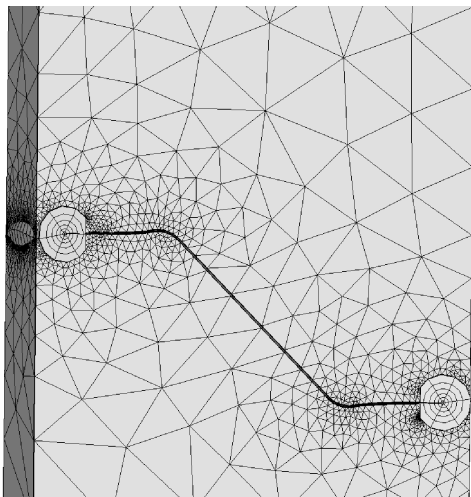


**Figure 1** : Mesh of the cracked Compact Tension Shear specimen

All previous actions are coded in the CRACKTRACER 3-D preprocessor. The result is a CalculiX input deck for

the cracked structure. The domain file limits the remeshing to a part of the structure. Since the newly generated hexahedral and tetrahedral meshes are usually more dense than the original mesh, specifying a domain limits the number of newly created elements and consequently the size of the cracked input deck. Furthermore, the user should try to define the crack domain in such a way that all loading and boundary conditions are external to the domain. This is important since the interpolation of the boundary conditions usually leads to additional inaccuracies.

Running CalculiX on the cracked input deck generates a file containing the stresses at the reduced integration points ahead of the crack front. The stress intensity factors are determined by comparing these stresses with the analytical expressions for the asymptotic stress field at the crack front [Dhondt (2002)]. Therefore, the method is also called the Quarter Point Element Stress method (QPES). This yields  $K_I$ ,  $K_{II}$  and  $K_{III}$  in each node along the crack front. By assuming that the crack propagation takes place in a plane orthogonal to the maximum principal asymptotic stress a deflection angle  $\varphi$  and a twist angle  $\psi$  can be determined [Dhondt (2003)]. The tensor obtained by multiplying the asymptotic stress tensor by  $2\pi\sqrt{r}$  is called the self-similar stress tensor. It has the same principal values as the asymptotic stress tensor but it has the dimension of stress intensity factor. The largest principal value of the self-similar stress tensor is interpreted as the equivalent stress intensity factor. It unites the effect of  $K_I$ ,  $K_{II}$  and  $K_{III}$  in one scalar. This scalar is used in a mode-I crack propagation law such as the Paris law to obtain the crack propagation velocity. Usually the number of cycles is determined for a fixed crack propagation increment, after which a new finite element calculation is performed. For this increment it is assumed that the K-values remain approximately constant. The size of the increment depends on the local curvature of the crack front. Indeed, for a large curvature the crack propagation increment should be rather small in order to capture the propagating crack accurately. The crack propagation increment is subsequently triangulated and joined with the crack triangulation of the previous increments. All actions following the CalculiX run are collected into the CRACKTRACER 3-D postprocessor. At that point a new crack front has been generated and the loop can start over again.

### 3 The center cracked tension specimen (CCT)

The center cracked tension specimen consists of a rectangular plate under tension with a central crack under 45° (Fig. 1). The width, length and thickness of the specimen are 48 mm, 96 mm and 12 mm, respectively. The total length of the initial crack is 24 mm. The Figure shows the crack at the end of the calculation. Clearly visible is the concentric hexahedral mesh surrounding the crack front and the tetrahedral mesh filling the space in the domain left after meshing the tubes. In total 22 iterations were performed. Due to the rather small size of the crack iterations the resulting tetrahedral mesh is also rather fine close to the crack extension.

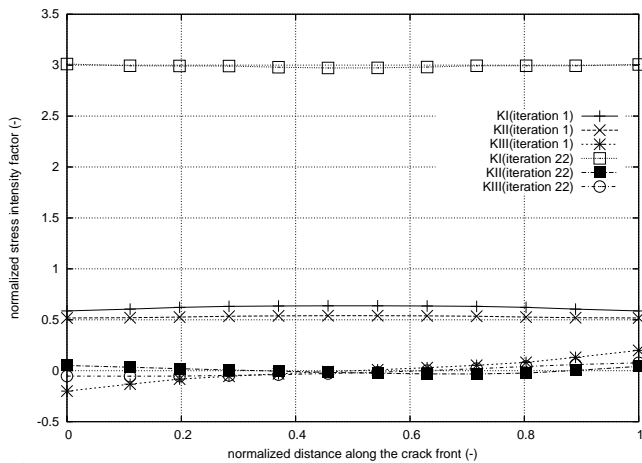


**Figure 2** : K-distribution along one of the crack fronts in the CCT specimen

The initial (iteration 1) and final (iteration 22) K-distribution is shown in Fig. 2. The values were normalized by  $\sigma\sqrt{\pi a}$ , where  $\sigma$  is the normal stress applied to the ends of the specimen and  $a$  is half the initial crack length. They agree very well with the values reported in [Dhondt, Chergui, and Buchholz (2001)]. This is not too surprising, since the same method (QPES) was used to determine the stress intensity factors, only the mesh is different. At the start of the calculation  $K_I$  and  $K_{II}$  are dominant and symmetric across the thickness,  $K_{III}$  is antisymmetry and rather small. The crack propagates in such a way that mode-I is favored, i.e. the crack twists until the loading is perpendicular to the crack face. This is clearly illustrated by the final K-distribution which is entirely dominated by  $K_I$ . Fig. 4 and Fig. 3 show the crack at the end of the calculation. It has propagated in a direction perpendicular to the loading and in a com-

pletely symmetric way, as was to be expected.

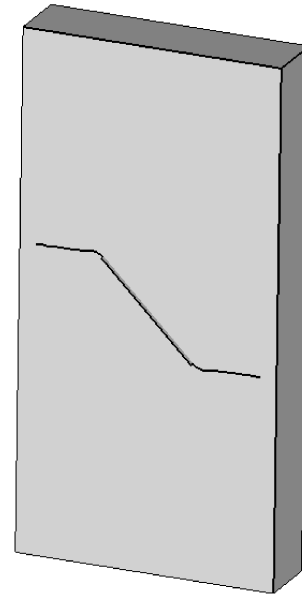


**Figure 3** : Final crack in the CCT specimen (shaded representation)

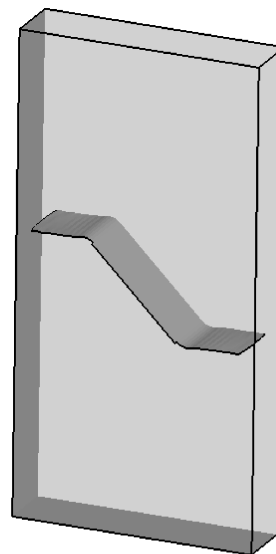


**Figure 4** : Final crack in the CCT specimen (front faces removed)

The crack length and the equivalent K-factor are shown in Fig. 5 and Fig. 6, respectively. The crack length at first increases in a linear way but accelerates substantially near the end of the calculation. This is typical for stress-induced crack propagation. This is also reflected in the

equivalent K-factor: due to the crack propagation the ligament which is left becomes smaller and is subject to a significantly higher stress. This leads to an increasing stress intensity factor and an even more strongly increasing crack propagation rate (the crack propagation rate is usually a quadratic or even higher order function of the stress intensity factor).

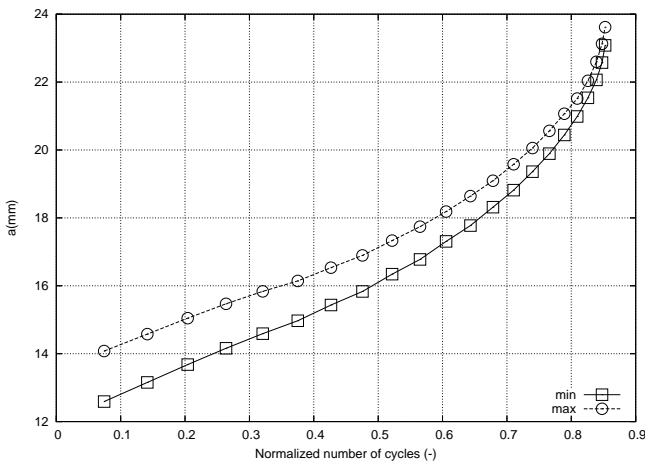


Figure 5 : Crack length during propagation

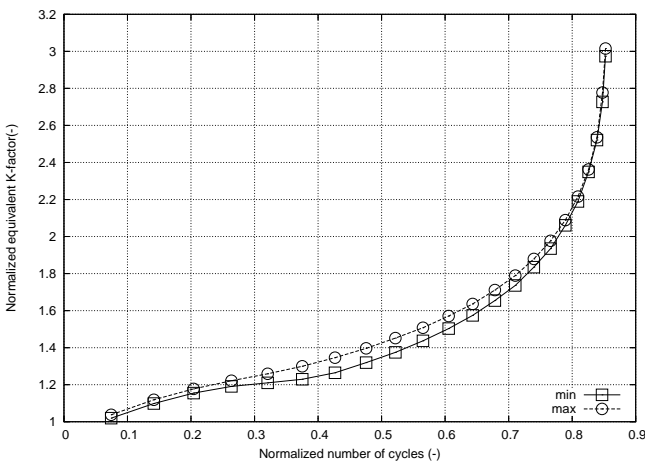


Figure 6 : Normalized equivalent K-factor during propagation

#### 4 The single edge notch specimen (SEN)

The geometry of the SEN specimen with initial crack is shown in Fig. 7. The length (x-direction) is 100 mm, the height (z-direction) is 50 mm and the thickness (y-direction) is 50 mm. A plane crack with straight crack front is introduced halfway the height. Its length is 50

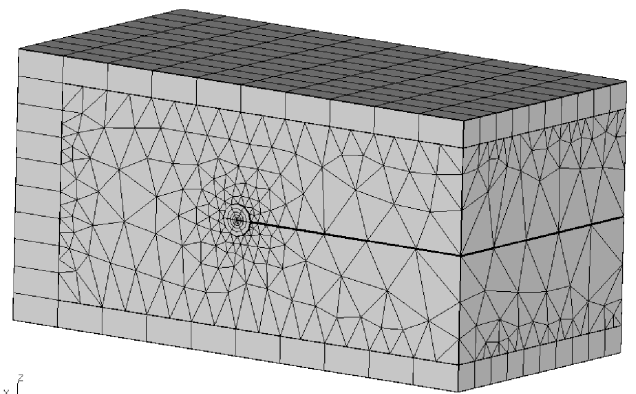
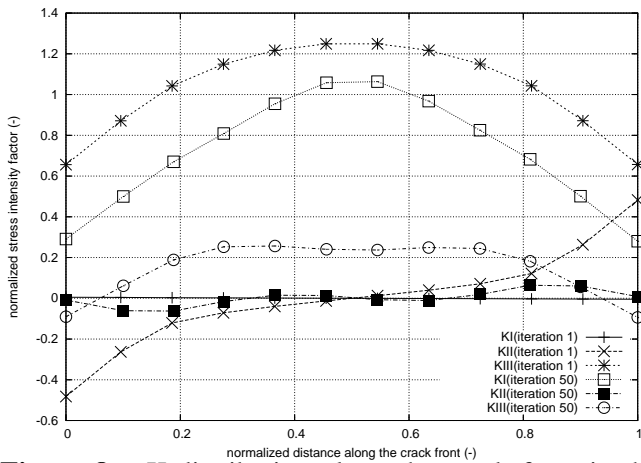


Figure 7 : Mesh of the SEN specimen with initial crack

mm. At the top of the specimen a uniform displacement is applied in y direction, whereas the bottom is fixed in all directions. The applied displacements essentially lead to mode-III loading at the crack front, although a substantial mode-II component also arises due to mode coupling. The coupling of mode-II and mode-III originates from the intersection of the crack front with the free surface.

In Fig. 7 the different regions of the cracked mesh are clearly visible. Along the top, bottom, and left side of the specimen one layer of brick elements is left over from the uncracked mesh. It is on this part that the boundary conditions are applied. By excluding these elements from the crack domain (the crack domain is defined as an element set that must be provided by the user) they are not modified by the preprocessor and any boundary conditions and loadings do not have to be interpolated on the new mesh. This reduces the computational time and increases the accuracy. The crack domain is remeshed in two regions: clearly visible is the tube with a focussed hexahedral mesh along the crack front. The remaining part of the crack domain was filled with tetrahedra. The mesh in the crack domain is completely independent from the original mesh in the uncracked structure. All three meshes (the elements kept from the uncracked mesh, the hexahedral mesh in the tube and the tetrahedral mesh elsewhere) are interconnected with linear multiple point constraints. Fig. 8 shows the initial and final K-distribution along the crack front. The K-values were normalized by  $\tau\sqrt{\pi a}$ , where  $\tau$  is the mean xy shear stress at the bottom of the specimen with initial crack and  $a$  is the initial crack length. A total of 50 iterations was performed. At the start of the calculation  $K_I = 0$ ,  $K_{III}$  is positive and sym-



**Figure 8 :** K-distribution along the crack front in the SEN specimen

metric while  $K_{II}$  is antisymmetric through the thickness. As specified before, the intersection of the crack front with the free surface leads to the mode-II/mode-III coupling. The initial K-distribution agrees very well with the results obtained in [Dhondt, Chergui, and Buchholz (2001)]. At the end of the calculation mode-I is dominant, while  $K_{II}$  is virtually zero. The  $K_{III}$  values have decreased by about 80%. In this context it should be mentioned that the deflection angle  $\varphi$ , which is essentially triggered by mode-II is fully taken into account during propagation, while the twist angle  $\psi$  is not taken into account. Indeed, it is not possible to incorporate the twist in the propagating crack surface without dropping continuity requirements. Backed by observations on the crack propagation in three point bending specimens, it is argued that mode-III leads to discontinuous crack faces reminding of factory roofs [Suresh (2003)]. Therefore it is not surprising that mode-III does not completely disappear during propagation.

The rather complicated crack propagation surface is shown in Fig. 10 and Fig. 9. It is antisymmetric, which agrees with the antisymmetric nature of mode-II. Due to the high  $K_{II}$  values at the free surface the curvature of the crack is very strong in these areas, but decreases while propagating. At the end of the calculation mode-II has virtually ceased to exist and the crack curvature tends to zero. Please note that the size of the initial crack was extended beyond the boundaries of the specimen out of technical remeshing reasons. The authors do not know of any experimental results involving this specimen but hope that the present results may encourage colleagues

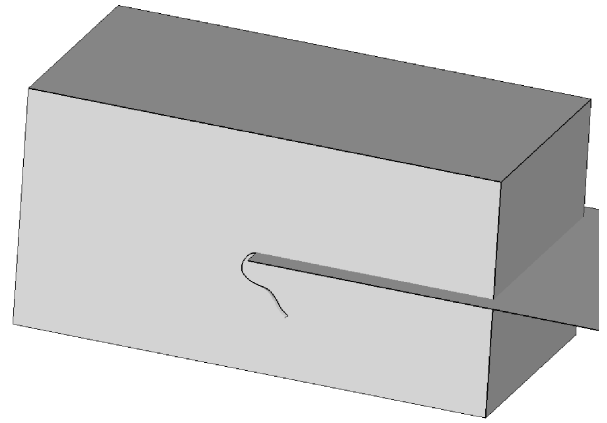


**Figure 9 :** Final crack in the SEN specimen (shaded representation)

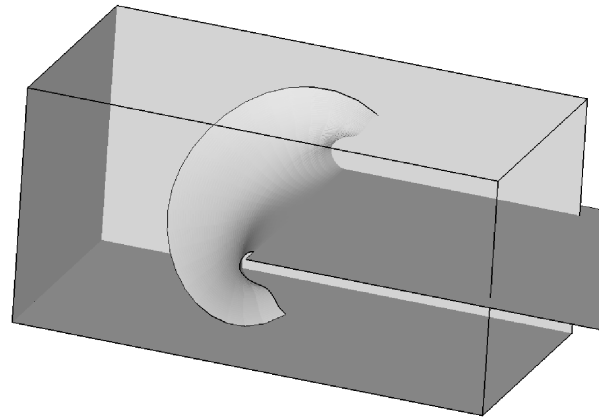


**Figure 10 :** Final crack in the SEN specimen (front faces removed)

to perform tests. Fig. 11 provides some insight on how the tube looks like at the end of the calculation. In this picture the mesh of the tube and the propagating surface is superimposed by the mesh of the front surface of the specimen. The tube surface sticks partly out of the specimen. This is not deemed to represent a problem since these parts of the tube will tend to be stress-free.

Fig. 12 shows the crack length versus the normalized number of cycles. Since the crack front is not circular, the crack length varies along the crack front. The crack length at a point along the crack front is defined as the Euclidean distance from that point to a reference point defined by the user. For the SEN specimen the center of the right-hand face in Fig. 9 was chosen as refer-

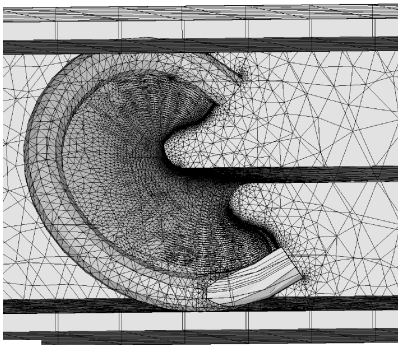


**Figure 11** : Tube surrounding the final crack front in the SEN specimen

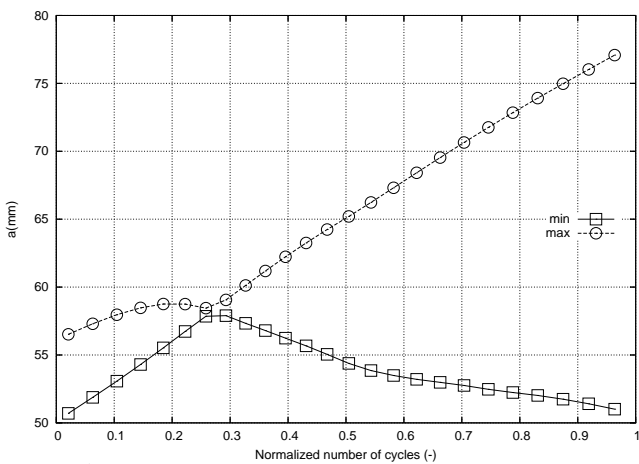


**Figure 12** : Crack length during propagation

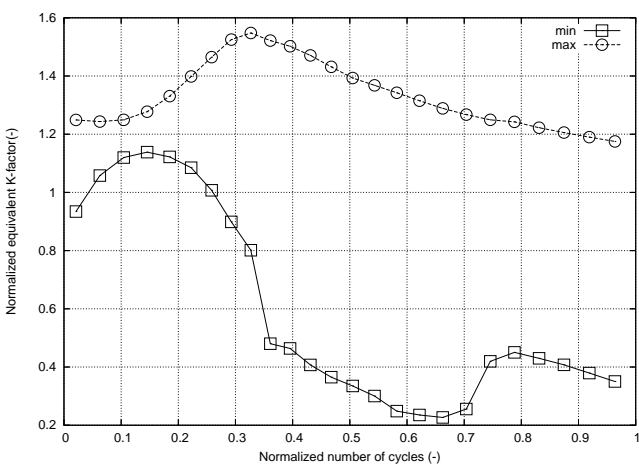


**Figure 13** : Normalized equivalent K-factor during propagation

ence point. Therefore, the minimum crack length along the initial crack front is 50 mm, the maximum distance

is  $\sqrt{50^2 + 25^2} = 55.9$  mm. The propagation of a point in the middle of the crack front is relatively linear, i.e.  $K$  is relatively constant. Indeed, in the symmetry plane there is no a  $K_{II}$  contribution which need to be converted into curvature and so the propagation at that point is really a conversion of  $K_{III}$  into  $K_I$ . Since the loading is displacement-driven crack propagation rather leads to a relaxation and no crack propagation peak is observed. The propagation at the free surface at first slightly increases, but subsequently it decreases as the  $K_{II}$  contribution is converted into curvature of the crack. This is also illustrated in Fig. 13: the upper curve represents the  $K_{equivalent}$  value in the center of the crack front. After a small rise it stays fairly constant. The equivalent stress intensity factor at the free boundary, though, decreases quite significantly.

**5 The quarter circular corner crack specimen (QCCC)**

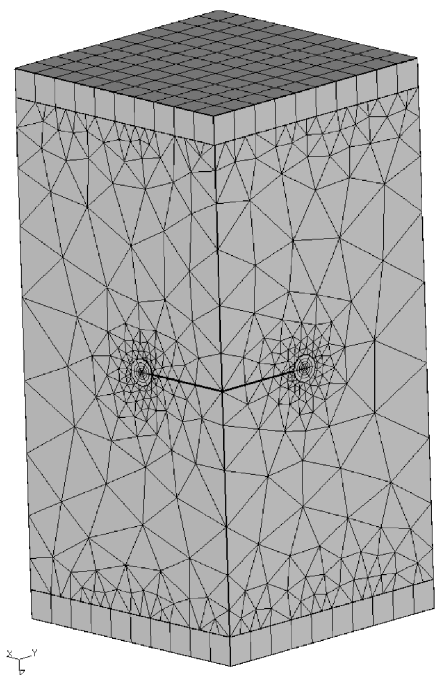


**Figure 14** : Mesh of the QCCC specimen with initial crack

The mesh of the QCCC specimen with initial crack is shown in Fig. 14. The size of the specimen is  $100 \times 100 \times 200$  mm<sup>3</sup> and the radius of the initial crack is 40 mm. The upper surface of the specimen is fixed in all directions. The lower surface is uniformly moved in

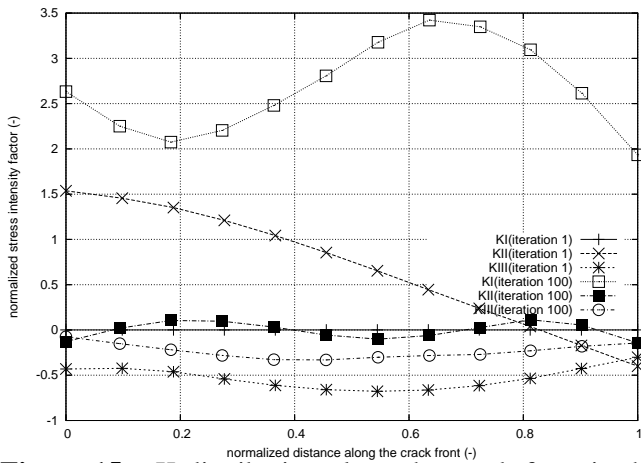


**Figure 15** : K-distribution along the crack front in the QCCC specimen

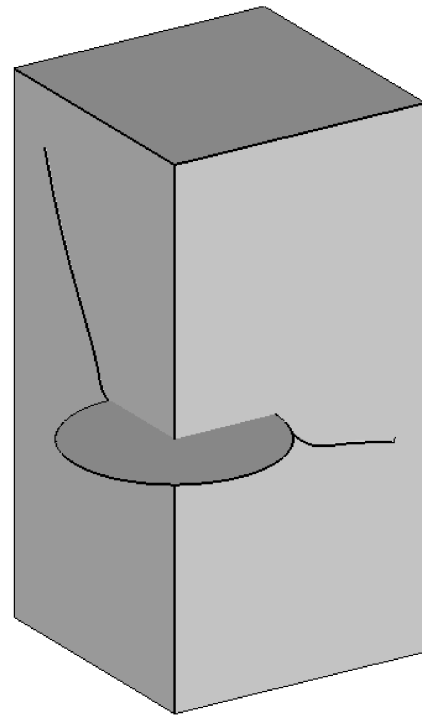
x-direction while the displacements in y and z-directions are zero.

The initial and final (after 100 iterations) K-distribution is depicted in Fig. 15. The forced displacements lead to mode-II at one end of the crack front and mode-III at the other end. However, due to mode coupling all shear modes are more or less activated: for small values of the normalized distance mode-II is dominant, mode-III is subdominant (values about 70 % less). At the other end of the crack front, where macroscopically mode-III prevails, the induced mode-II values even exceed the mode-III ones. Mode-I is zero. At the end of the calculation mode-I clearly dominates, mode-II is nearly zero and mode-III has been reduced by about 50 %.

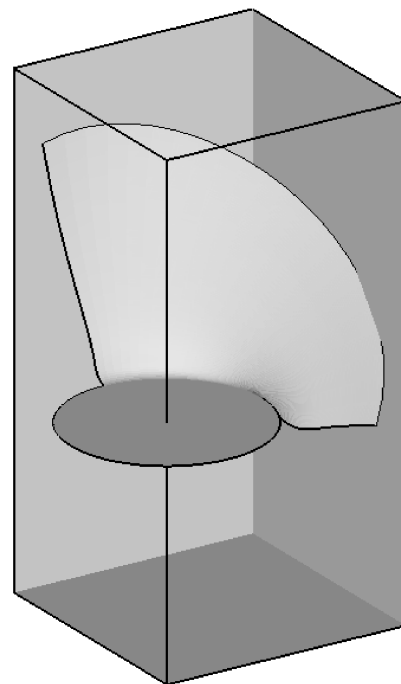
The crack propagation ( Fig. 17 and Fig. 16) follows well-known patterns. At the side predominantly loaded by mode-II the crack surface veers off at an angle of 64°, which is close to the 70° you would expect for pure mode-II. At the opposite side the crack grows in the reverse direction ( $K_{II}$  has a different sign) but soon turns into a horizontal plane. The whole crack surface is smoothly curved.

Fig. 18 shows the triangulation of the initial crack (extended as a full circle) and the crack increments. The small increments allow for an accurate representation of the strongly curved crack faces.

Finally, Fig. 19 and Fig. 20 show the crack length and the equivalent K-factor as a function of the normalized number of cycles. The reference point for the crack length measurements was the center of the initial (part) circular



**Figure 16** : Final crack in the QCCC specimen (shaded representation)



**Figure 17** : Final crack in the QCCC specimen (front faces removed)

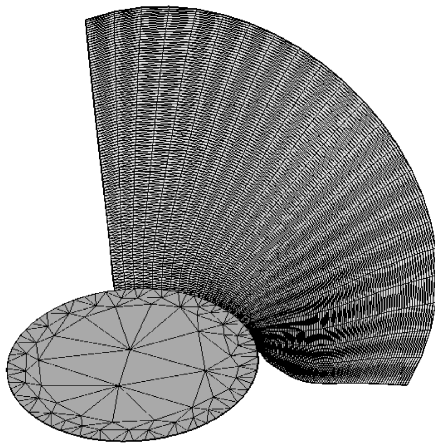


Figure 18 : Triangulation of the crack propagation increments in the QCCC specimen

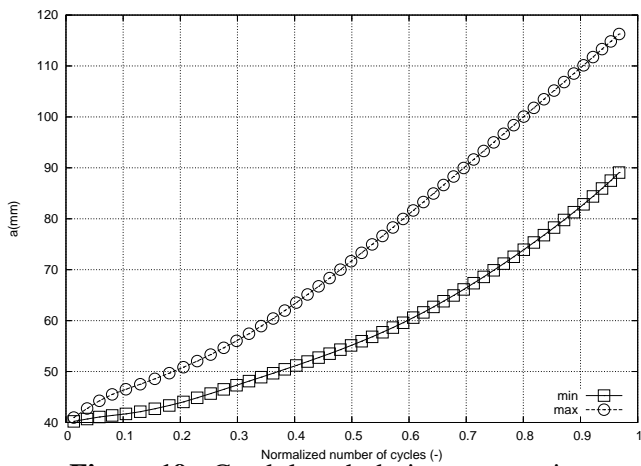


Figure 19 : Crack length during propagation

crack. The maximum curves correspond to the side of the crack front which is predominantly subject to mode-II.

### 6 Three point bend specimen (3pb)

The geometry of the three point bending specimen is shown in Fig. 21. It is 300 mm long, 20 mm thick and 60 mm high. A line load of 300 N/mm is applied on the top of the specimen in the middle. The distance between the line supports at the bottom of the specimen is 240 mm. An initial crack with length 11 mm making an angle of 45° was introduced along the lower edge. This is not identical with the calculation in [Dhondt, Chergui, and Buchholz (2001)] (where the initial crack length was 20 mm), however, the results should be qualitatively simi-

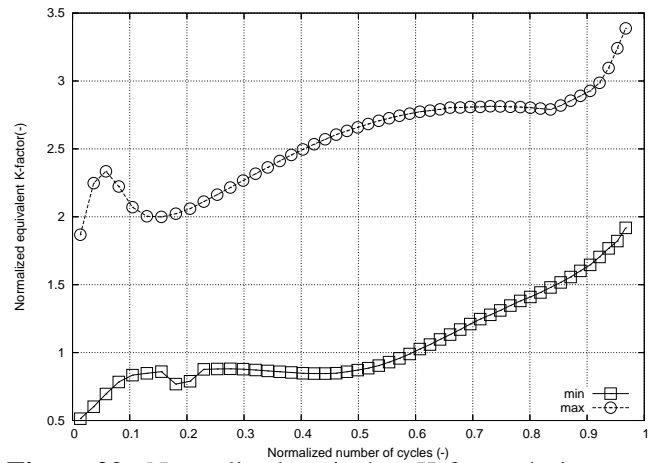


Figure 20 : Normalized equivalent K-factor during propagation

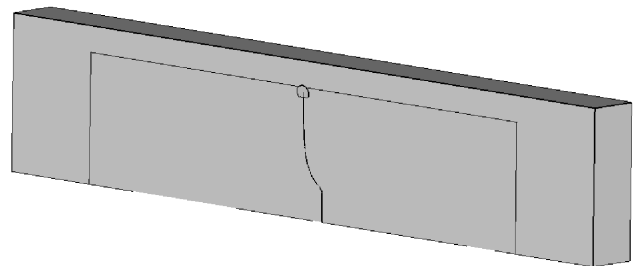


Figure 21 : Geometry of the 3pb specimen with initial crack

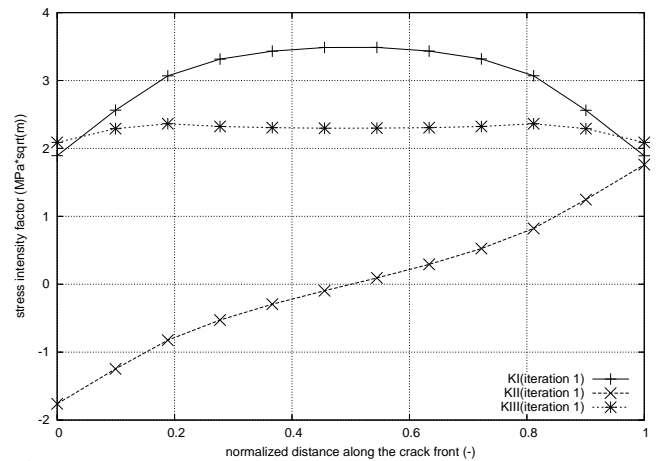
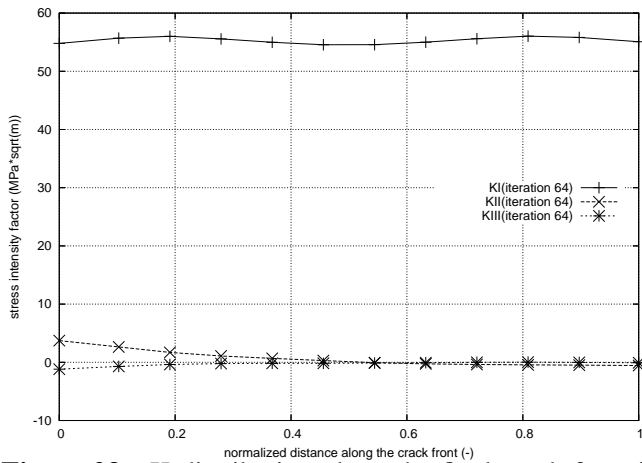
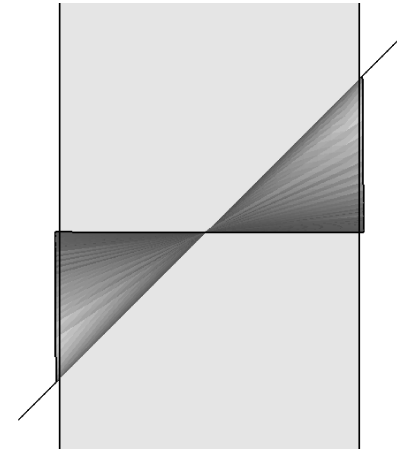


Figure 22 : K-distribution along the initial crack front in the 3pb specimen

lar. The picture shows the domain (outlined by a continuous line), the initial crack and the propagation of the crack. The circle represents the tube at the end of the



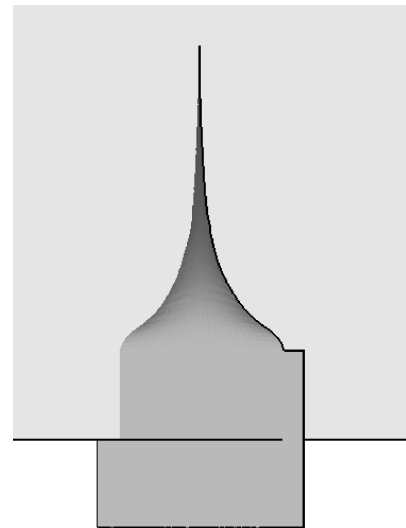
**Figure 23 :** K-distribution along the final crack front in the 3pb specimen



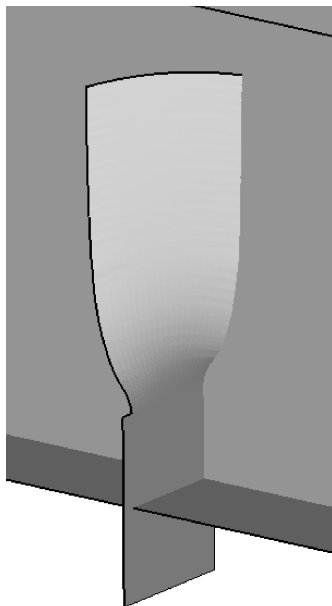
**Figure 25 :** Final crack in the 3pb specimen (view from above)

calculation. It is clear that the crack propagation cannot leave the crack domain. If more crack propagation is requested, the domain has to be adapted appropriately.

The stress intensity factor distribution is shown in Fig. 22 and Fig. 23. The applied loading leads to a bending moment, a torque and shear forces in the crack plane. This results in mode-I, mode-II and mode-III.  $K_I$  and  $K_{III}$  are symmetric along the crack front,  $K_{II}$  is antisymmetric. At the end of the calculation, after 64 iterations,  $K_I$  is clearly dominant.



**Figure 26 :** Final crack in the 3pb specimen (frontal view)



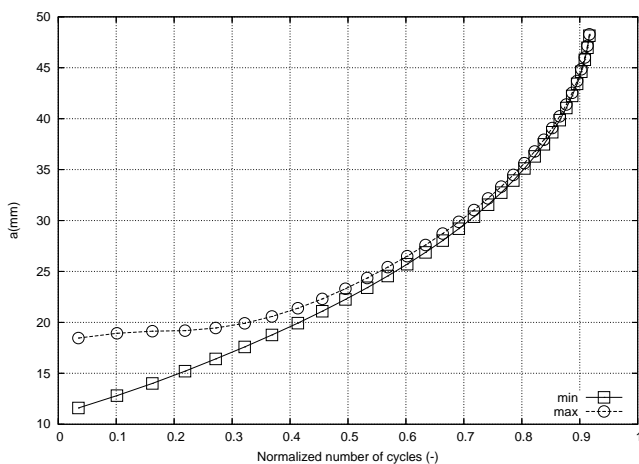
**Figure 24 :** Final crack in the 3pb specimen (front faces removed)

Fig. 24, Fig. 25 and Fig. 26 show the propagated crack surface. The crack grows gradually into the symmetry plane, as was to be expected. This also agrees with experimental evidence [Dhondt, Chergui, and Buchholz (2001)], [Dhondt (2004)]. The main difference with the experiments is that the calculation predicts a smooth crack surface, whereas the real crack surfaces exhibit a factory roof effect (Fig. 27; this was really a four-point bending test, the effect, however, is the same): this is generally attributed to a mode-III effect [Theilig (2008)] [Suresh (2003)]. Since the calculations operate with continuous surfaces, this effect cannot be modeled



**Figure 27** : Crack propagation in a titanium four-point bending specimen

and may lead to some crack retardation in the experiment.



**Figure 28** : Crack length during propagation

Finally, Fig. 28 and Fig. 29 show the crack length and the equivalent K-factor during propagation. The reference point for the crack length measurement was the center point of the lower surface of the specimen. Since the specimen loading is force-driven there is a clear increase of the K-factors towards the end of the calculation.

## 7 Conclusions

A new method has been presented to calculate mixed-mode cyclic crack propagation with the finite element

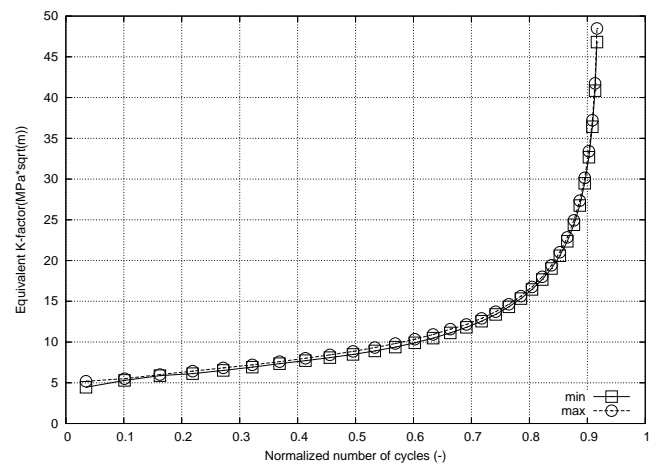


**Figure 29** : Equivalent K-factor during propagation

method in a fully automatic way. Qualitatively the results agree with common sense and with the few available experiments in the field. First applications to aircraft engine parts have shown that the method is stable, fast and capable of taking the detailed geometry and loading conditions of complex parts into account.

## References

- Barsoum, R.** (1976): On the use of isoparametric finite elements in linear fracture mechanics. *Int. J. Numer. Meth. Engng.*, vol. 10, pp. 25–37.
- Belytschko, T.; Lu, Y. Y.; Gu, L.** (1994): Element-free Galerkin method. *Int. J. Numer. Meth. Engng.*, vol. 37, pp. 229–256.
- Bremberg, D.; Dhondt, G.** (2008): Automatic crack-insertion for arbitrary crack growth. *Engng. Fract. Mech.*, vol. 75, pp. 404–416.
- Bremberg, D.; Dhondt, G.** (2009): Automatic 3-D crack propagation calculations: a pure hexahedral element approach versus a combined element approach. *Int. J. Frac.*, vol. 157, pp. 109–118.
- Dhondt, G.** (2002): Mixed-mode K-calculations in anisotropic materials. *Eng. Fract. Mech.*, vol. 69, pp. 909–922.
- Dhondt, G.** (2003): A New Three-Dimensional Fracture Criterion. *Key Engng. Mater.*, vol. 251-252, pp. 209–214.

**Dhondt, G.** (2004): Versuchsergebnisse von Titan 4-Punkt Biegeproben mit schrägem Anfangsriss bei hoher Temperatur. *DVM-Bericht "Fortschritte in der Bruch- und Schädigungsmechanik"*, , no. 236, pp. 163–170.

**Dhondt, G.; Chergui, A.; Buchholz, F.-G.** (2001): Computational fracture analysis of different specimens regarding 3D and mode coupling effects. *Eng. Fract. Mech.*, vol. 68, pp. 383–401.

**Dhondt, G.; Wittig, K.** (1998–2010): CalculiX, a Free Software Three-Dimensional Structural Finite Element Program. [www.calculix.de](http://www.calculix.de).

**Helldörfer, B.** (2009): *Ein randelementbasiertes 3D-Rissfortschrittsmodul für Finite Elemente Systeme*. VDI Verlag.

**Melenk, J. M.; Babuska, I.** (1996): The Partition of Unity Finite Element Method: Basic Theory and Applications. *Comput. Meth. Appl. Mech. Engng.*, vol. 139, pp. 289–314.

**Murakami, Y.** (1987): *Stress intensity factors handbook*. Pergamon Press, Oxford.

**Schöberl, J.** (1997): NETGEN - An advancing front 2D/3D-mesh generator based on abstract rules. *Comput. Visual. Sci.*, vol. 1, pp. 41–52.

**Suresh, S.** (2003): *Fatigue of Materials*. Cambridge University Press, United Kingdom.

**Theilig, H.** (2008): Die Anwendung der FKM-Richtlinie zur Bruchmechanischen Festigkeitsbewertung von Maschinenbauteilen bei Mixed-Mode-Beanspruchung. *DVM-Bericht "Fortschritte in der Bruch- und Schädigungsmechanik"*, , no. 240, pp. 191–?

**Wen, P. H.; Aliabadi, M. H.** (2010): Mixed-mode Stress Intensity Factors by Mesh Free Galerkin Method. *Key Engng. Mater.*, vol. 417-418, pp. 957–960.

